Scripta Materialia 197 (2021) 113791

Contents lists available at ScienceDirect

Scripta Materialia

journal homepage: www.elsevier.com/locate/scriptamat

Unveiling interactions of non-metallic inclusions within advanced ultra-high-strength steel: A spectro-microscopic determination and first-principles elucidation

Harishchandra Singh[a,*], Tuomas Alatarvas[b,*], Andrey A Kistanov[a], S Assa Aravindh[a], Shubo Wang[a], Lin Zhu[c], Brice Sarpi[c], Yuran Niu[c], Alexei Zakharov[c], F.M.F. de Groot[d], Marko Huttula[a], Wei Cao[a,*], Timo Fabritius[b]

[a] Nano and Molecular Systems Research Unit, Centre for Advanced Steels Research, University of Oulu, FIN-90014, Finland
[b] Process Metallurgy Research Unit, Centre for Advanced Steels Research, University of Oulu, FIN-90014, Finland
[c] MAX IV Laboratory, Lund University, Lund 22484, Sweden
[d] Debye Institute for Nanomaterials Science, Utrecht University, Universiteitsweg 99, CG Utrecht 3584, the Netherlands

ARTICLE INFO

Article history:
Received 22 December 2020
Accepted 7 February 2021
Available online 13 February 2021

Keywords:
Non-metallic inclusion
Ultra-high-strength steel
Synchrotron spectro-microscopy
X-ray absorption spectroscopy
DFT

ABSTRACT

Determining non-metallic inclusions (NMIs) are essential to engineer ultra-high-strength steel as they play decisive role on performance and critical to probe via conventional techniques. Herein, advanced Synchrotron X-ray absorption coupled with photoemission electron microscopy and first-principles calculations are employed to provide the structure, local bonding structure and electronic properties of several NMI model systems and their interaction mechanism within and the steel matrix. B K-, N K-, Ca $L_{2,3}$- and Ti $L_{2,3}$-edge spectra show that the additional B prefers to result in h-BN exhibiting strong interaction with Ca^{2+}. Such Ca^{2+}-based phases also stabilize through TiN, revealing the irregular coordination of Ca^{2+}. Observed intriguing no interaction between TiN and BN is further supported with the first-principles calculations, wherein unfavorable combination of TiN and h-BN and stabilization of bigger sized Ca^{2+}-based inclusions have been found. These observations can help to optimize the interaction mechanism among various inclusions as well as steel matrix.

Determining non-metallic inclusions (NMIs) in ultra-high-strength steel (UHSS) has been a crucial step for clean steel as steel is the most used metal in industry and civil life. However, the inclusions, in particular, their composition, size, shape, and amount, can create serious problems like breakage of steel wires during drawing, hydrogen-induced cracking, fatigue failure, and surface flaws [1–4]. NMIs are regions of non-metallic chemical compounds, e.g., Al_2O_3, SiO_2, $MgAl_2O_4$ (oxides), MnS, CaS (sulfides), and AlN, BN, TiN (nitrides) within a steel matrix that are formed through various physical effects during the different stages of steel production. These inclusions can have a significant effect on the mechanical properties and quality (toughness, durability, machinability, fatigue, formability and corrosion resistance) of the steel product [5,6]. Therefore, identifying the critical size, shape, structure of NMIs is important for controlling the properties of steels.

Studies of NMIs require experimental and theoretical dedications. Various nondestructive characterizations have been emphasized on microscopic determinations on their morphologies with element specifications [1–3]. Electrolytic extraction is performed to dissolve the steel matrix around an inclusion and perform imaging [7]. However, this method is partially destructive due to possible dissolution of inclusions. Recently, cathodoluminescence and 3D X-ray computed tomography have also been implemented [8,9]. However, conventional methods fail to provide chemical information of small-sized NMIs. Alternatives are sought within modern characterization tools especially engaging advanced photon sources. Particularly, X-ray absorption (XAS)-photoemission electron microscopy (PEEM), referred as X-PEEM, is a method to generate detailed images based on the XAS spectrum. The high sensitivity of XAS spectrum to chemical composition, phase transition, and effect of surrounding environment makes X-PEEM a highly attractive. Changes in XAS spectrum at spatially different position can be monitored to offer simultaneous microscopy and spectroscopy. Theoretically, interaction mechanisms of NMIs need clarifications

* Corresponding authors.
E-mail addresses: harischandra.singh@oulu.fi (H. Singh), tuomas.alatarvas@oulu.fi (T. Alatarvas), wei.cao@oulu.fi (W. Cao).

https://doi.org/10.1016/j.scriptamat.2021.113791

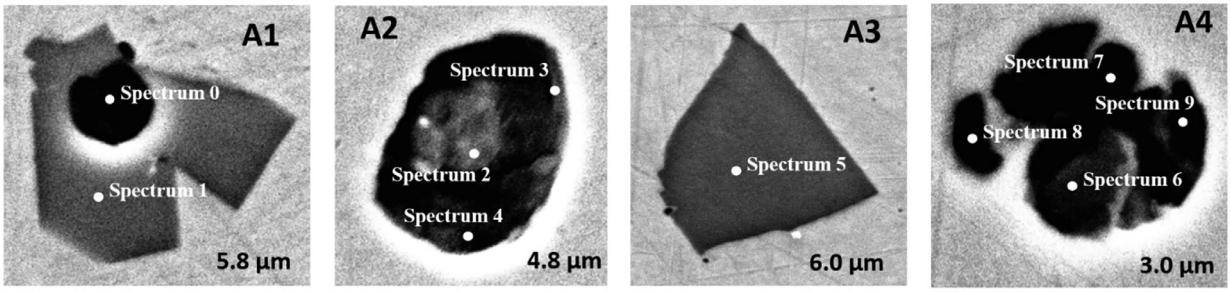

Fig. 1. Various inclusions identified by SEM. The corresponding elemental distribution is analyzed by EDS map of the same (Table S2, Figs. S4 and S5).

at quantum mechanical levels. Density functional based theory (DFT) calculations is a powerful supporting tool, for instance, joint experimental and DFT study revealed the effect of various inclusions on the performance of steel [10–13], indicating its potential when coupled with advanced spectro-microscopy (X-PEEM).

Herein, we present a systematic spectro-microscopic determination of commonly observed NMIs within the steel matrix along with DFT to elucidate their interaction and formation mechanism. The combination of experimental and DFT-based computational methods presented here provide better contrast for the elements present within the inclusions due to the phase/work function contrast giving chemical / elemental information about the inclusion, matrix and the boundary, or the interface.

The sample is a commercial low-alloyed carbon steel with a nominal composition of 0.15C, 0.3Si, 1.0Mn, 0.4Cr in wt.%. Its phase and micrograph were recorded via high energy synchrotron X-ray diffraction (HE-SXRD, Fig. S1), and FESEM-EDS (Figs. S2, S4 and S5). The X-PEEM was carried out at MAXPEEM beamline of the MAX IV laboratory (Lund, Sweden). Incident beam has a 2×10^{-4} bandwidth and photon flux $\approx$ 1-5 $\times$ 10^{12} ph/s (200-900 eV). A modified SX-700 monochromator with Au/Si 300 or 1200 -line/mm grating was used to probe the B K-edge, N K-edge, Ti $L_{2,3}$-edge and Ca $L_{2,3}$-edge XAS. The incident photon energy was scanned at a 0.2 eV step for all edges except for the Ti $L_{2,3}$ at a 0.1 eV step. At each energy, a secondary-XPEEM image was recorded with a TVIPS F-216 optical fiber-coupled CMOS detector with 2 $\times$ 2 binning, providing a 1024 $\times$ 1024 pixels resolution over the 25 μm field of view. The acquisition parameters were set as 0.2 s exposure and 16 frames averaging per image. More details can be found in our previous studies [14]. The computational part was carried out in the framework of DFT using the plane wave pseudopotential code, Vienna Ab initio Simulation Package [15]. To simulate the non-metallic inclusions, clusters are modeled using the cubic super cell approach. The geometry optimization of all clusters was treated based on the Perdew-Burke-Ernzerhof (PBE) functional within the generalized-gradient approximation (GGA) [16], to comprise accuracy and computational cost [17]. Further details are provided in the supplementary document along with Fig. S3.

Fig. 1 depicts SEM images of four inclusions of interests. They are embedded in a steel bulk whose phases and micrograph were first investigated through HE-SXRD and laser microscopy (Figs. S1 and S2). Table S1 summarizes phases detected in these inclusions. In addition to the major ferrite phases, a small amount of retained austenite and cementite phase can also be found. In such a steel, NMIs of ppm-level concentration [18,19] can hardly be detected by the HE-SXRD which determine microstructures of the bulk. The inclusion length is noted in Fig. 1. SEM–EDS mapping analysis, which only gives elemental information is also presented (Figs. S4 and S5, Table S2). The selected inclusions are mostly Ti, B and Ca-based compounds. Particularly, inclusions A1 and A3 contain Ti-based compounds, A2 and A4 on the other hand mainly contain Ca- and B-based compounds. To get insight information, the above elements are investigated with chemical distinctions at microregions [14,20]. Analysis also includes calibrations with the published data, e.g. Ti $L_{2,3}$-edge [21].

Fig. 2 shows X-PEEM view of A1 and A3 inclusions along with Ti $L_{2,3}$-edge XAS spectra from various selected locations. The corresponding 3D surface plot clearly shows the presence of different types of inclusions in A1, indicating one type is surrounded by the other type. Ti $L_{2,3}$-edge XAS probes the unoccupied 3d states of Ti via electron transitions from spin orbit split levels $2p_{3/2}$ to 3d (L_3-edge) and $2p_{1/2}$ to 3d (L_2-edge). Due to crystal field splitting L_3 and L_2-edges are further split into t_{2g} and e_g levels (shown in the inset for both the L_2 and L_3-edge via t1 to t4). The energy separation between the peaks in the L_3 and L_2-edge is ~ 1.2 eV and ~1 eV, respectively. Fig. 2c and d shows similar results of TiN for inclusion A3. On comparing the XAS spectra including their tiny features with the reported Ti-based compounds, the results indicate that in the present case, A1 and A3 inclusions show the characteristics of TiN [21,22], which is further confirmed with N K-edge XAS data discussed below.

Fig. 3a–d shows the X-PEEM views and the corresponding N K-edge XAS spectra along with the TiN reference. The N K-edge XAS can be divided into two regions: the doublet at threshold (n1 and n2), and the broader structure (n3 and n4). The first region is attributed to unoccupied N 2p states which are hybridized with Ti 3d bands. These bands further split by crystal field effects into the t_{2g} and e_g sub-bands (shown in pairs via n1 to n4). The second region at higher energies is attributed to unoccupied N2p states which are hybridized with Ti 4sp bands. The first region presents weak dispersion effects; the width of each sub-band is of the order of 2.5 eV. The second region presents larger dispersion effects (4.5 eV) and is more sensitive to long range order, suggesting that the observed N K-edge XAS spectra match with that of TiN [21,22].

Fig. 4 depicts the X-PEEM image and corresponding Ca $L_{2,3}$-edge XAS spectra for inclusions A1, A2 and A4, along with various references. Absence of XAS signal for inclusion A3 indicates that there are no Ca-containing phases (Table S1). Two sharp peaks in the energy range 345-255 eV essentially show Ca^{2+} characteristics, while a peak at ~356 eV is probably an experimental artifact (second harmonics of Fe). A typical Ca $L_{2,3}$-edge XAS spectrum contains several features which are a result of the combination of spin–orbit and crystal-field splitting [23,24] . The two major peaks, L_3 ~350.2 eV (a2) and L_2 ~ 353.6 eV (b2) are the result of the spin–orbit coupling. These peaks further crystal-field split into a triplet (t_{2g}) and a doublet (e_g), denoted as minor peaks (a1 ~ 349 eV and b1 ~ 352.5 eV) and a few leading peaks (1, 2, 3: Fig. 4g). Since the cause of crystal field splitting is the ligand (e.g., O and S) interaction with the central atom (i.e., Ca here), the intensity and position of these crystal-field split features are highly correlated to the coordination/symmetry. For instances, in case of perfect/closely octahedral symmetry, two major peaks are strongly split so that the intensities of the minor peaks are comparable to those of the major peaks (see the case of $Ca(OH)_2$, CaO, $CaCO_3$ in Fig. 4g) [25,26].

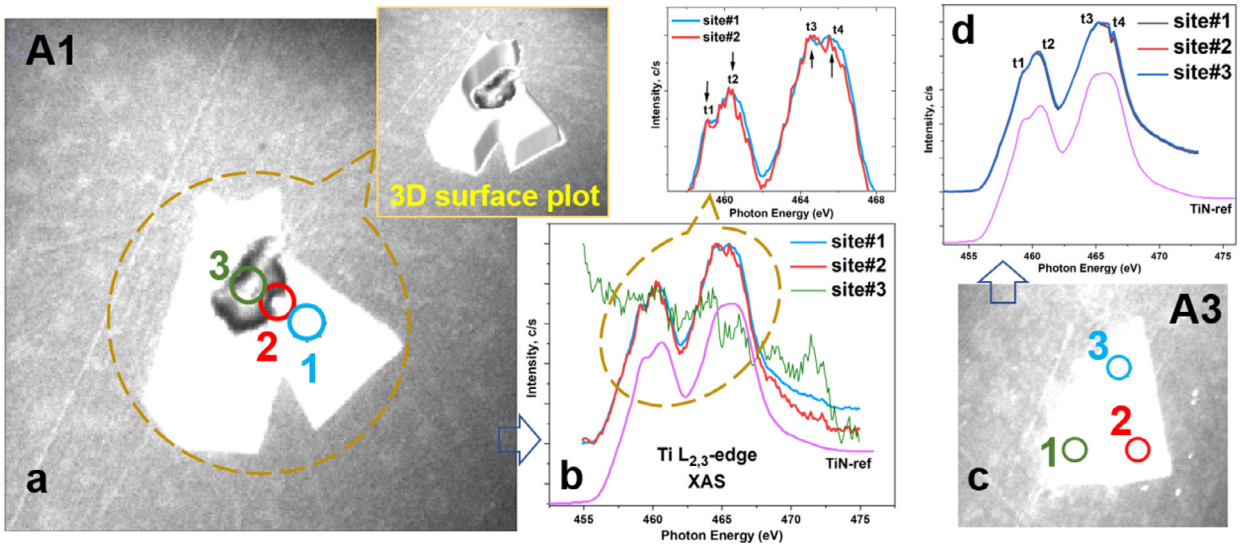

Fig. 2. (a and c) X- PEEM image, (b and d) Ti $L_{2,3}$-edge XAS spectra at various spatial positions as marked in a and c. Corresponding tiny features of Ti $L_{2,3}$-edge XAS spectra and 3D surface plot of a and b is also shown for clarity. Fig. 2c and d include Ti $L_{2,3}$-edge XAS spectra along with the TiN ref [21,22].

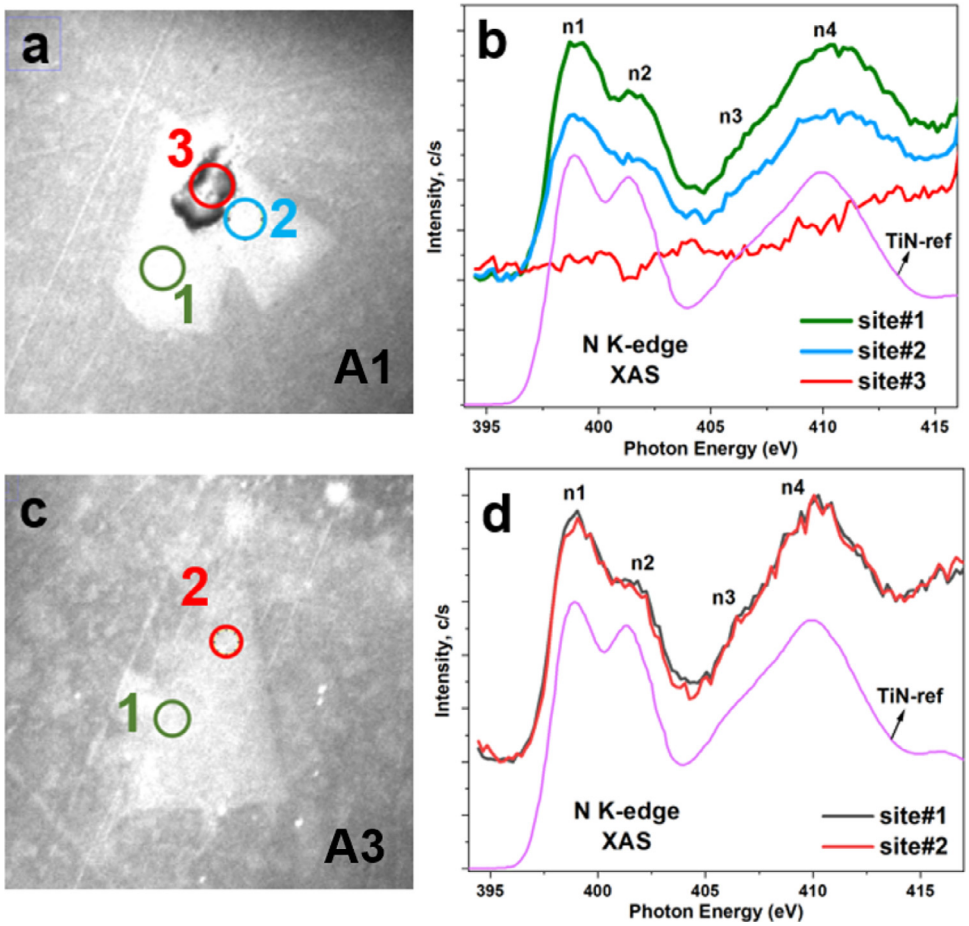

Fig. 3. (a and c) X-PEEM image, (b and d) N K-edge XAS spectra at selected positions marked in a and c. Fig. 3b and d also contain N K-edge XAS spectra along with the TiN reference.

Besides, significant energy differences between major and minor peaks are visible. These two behaviors jointly indicate strong crystal field effect, which also allows strong minor peaks with energy difference from adjacent major peaks of about 1.2–1.4 eV. The same features in the case of irregular coordination result in a weak crystal field. In this case, 3d orbital is less degenerated and minor peaks decrease in intensity and shift to higher energy. The latter effect makes the minor peaks less distinguishable, as the later effect also shortens the distance between major and minor peaks. Such observation has been used for the interpretation of Ca coordination status and the strength of the crystal field in various Ca-based compounds [25,26]. Therefore, the two sharp calcium peaks

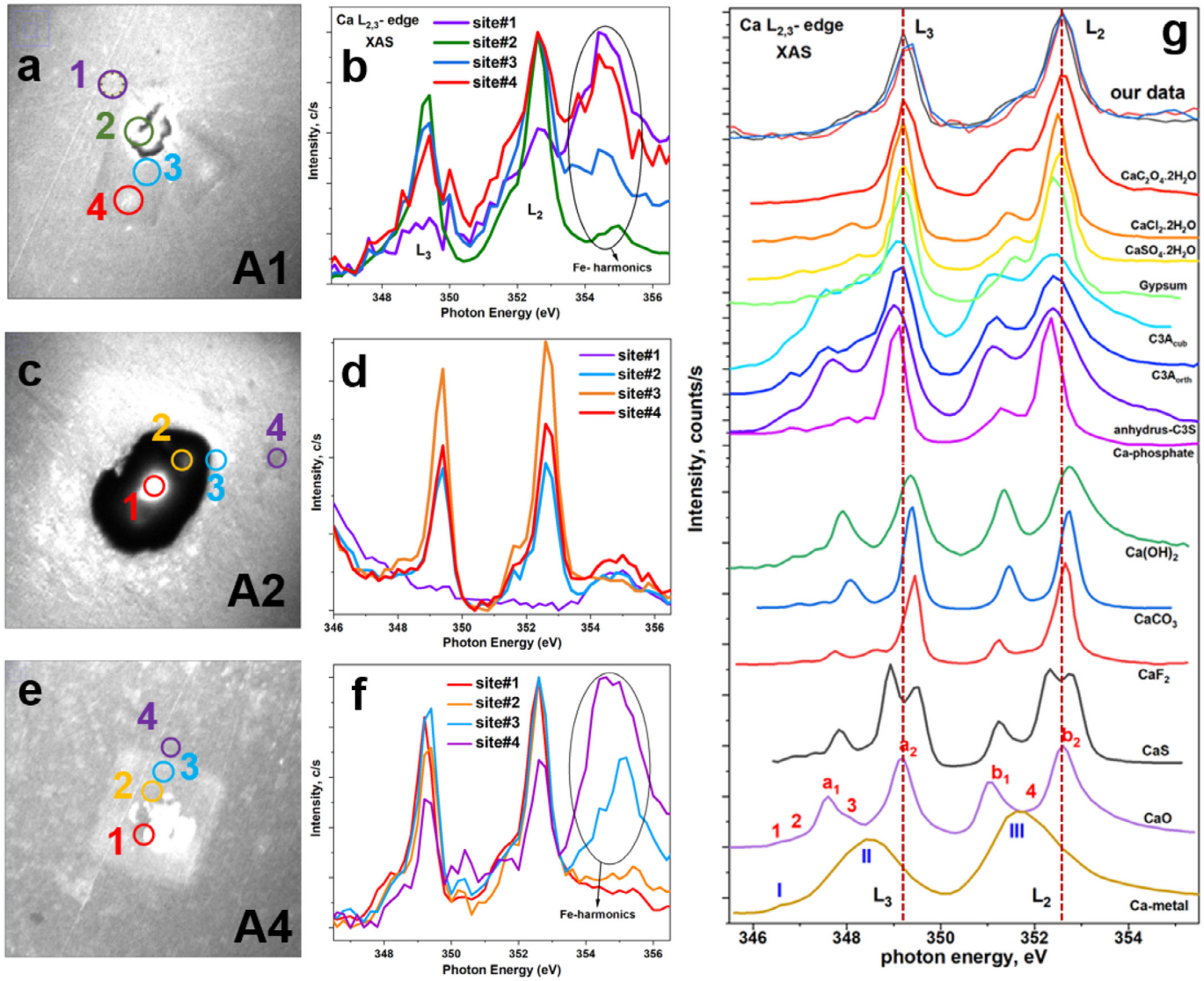

Fig. 4. (a, c and e) X-PEEM images of inclusions A1, A2 and A4. (b, d and f) Corresponding Ca $L_{2,3}$-edge XAS spectra at various spatial positions marked in a, c, e; and (g) reproduced Ca $L_{2,3}$-edge XAS spectra of various references along with a typical observed data.

essentially show Ca^{2+} with a relatively small crystal field, indicating poor symmetry of Ca^{2+}. It's worth pointing out that the major peaks are consistent among all spectra. Changes in chemical environment seems to be solely indexed by intensity and energy values of minor peaks. As seen from the analysis and previously published work, Ca can be stabilized in several possible coordination/phases. Nevertheless, the result of current analysis indicates that the observed divalent Ca-based inclusions stabilize in multiphase structure as well as via interaction with TiN or BN together with irregular coordination and a weak crystal field [23,24,27].

X-PEEM image and corresponding B K-edge XAS spectra are depicted in Fig. 5 for inclusions A1, A2 and A4. No B K-edge XAS signal appears in A1. However, A2 and A4 show significant signal of B K-edge XAS, corresponding to characteristics of h-BN. Three significant features are clearly resolved at the B K-edge XAS (Fig. 5d and f) numbered as b1, b2 and b3. Feature b1 (~193 eV) is the well-known π^*(2pz) resonance of h-BN. Higher energy b2 and b3 features are assigned to σ^* resonance of h-BN. From the molecular orbital perspective, the intense double feature ~ 199.5 eV and ~ 201 eV are due to localized σ^*(2px, 2py) antibonding between B and N. Furthermore, based on the band theory, they could be assigned to the transitions to the maximum density of states at the L/M and Γ point of the first Brillouin zone (BZ) of h-BN, respectively [28–30].

From the DFT-based analysis (Fig. S6, Table S3 and S4), NMIs with higher concentrations of Ti possess lower binding energy. This suggests formation of pristine BN inclusion or BN with a low content of Ti is more favorable, in consistent with the experimental data where most of the inclusions is either BN or TiN but not a combination of both. In addition, with increasing the Ti concentration the shape of the BN inclusion changes from spherical to ellipsoidal, the same result from binding energy perspective. Importantly, the volume of the pristine BN (323.83 $Å^3$) is ~2.2 times less than that of the pure TiN inclusion (727.76 $Å^3$). This agrees with the experimental results where the small spherical inclusions are mainly composed of BN while the large inclusions angular shape may include Ti. The similar tendency has also been noticed for CaS inclusion doped with Al i.e., with increasing Al concentration, the binding energy significantly decreases suggesting that the formation of pure CaAl or CaS with a low content of Al is more favorable. Comparing to the BN and BNTi, CaS, CaSAl, and CaAl inclusions possess much lower binding energy. Hence, the existence of CaS, CaSAl, and CaAl inclusion is more favorable. It should be noted the size of Ca-based NMIs is about 2 times larger than that of B-

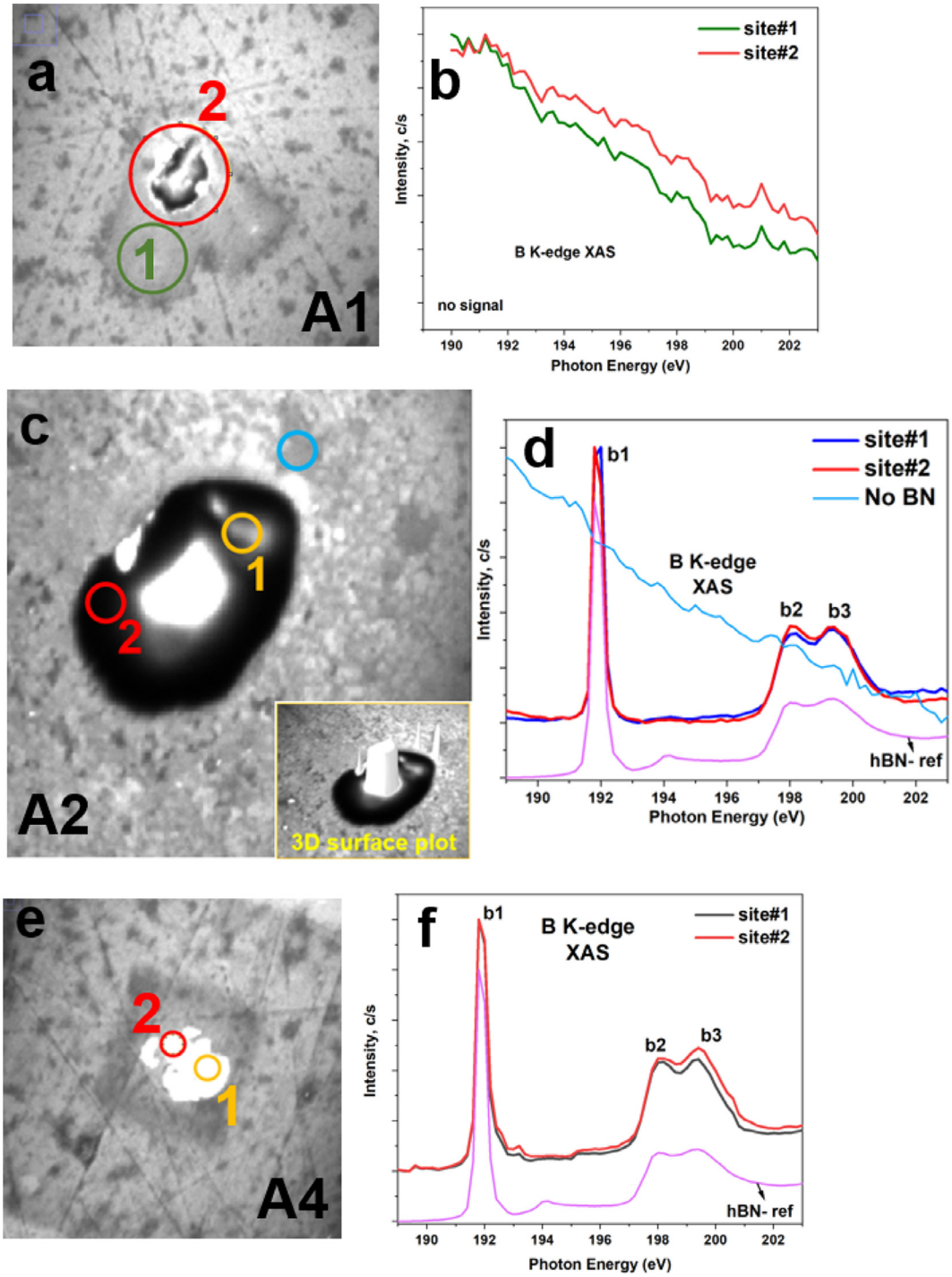

Fig. 5. (a, c and e) X-PEEM images for inclusions A1, A2 and A4. (b, d and f) Corresponding B K-edge XAS spectra marked in a, c, e. Fig 5c and d, f also show the corresponding 3D surface plot and h-BN.

based NMIs. These observations are also well consistent with our experimental data.

The complication of NMIs is elucidated in this dedicated work. Typical NMI phases in aluminum killed, calcium treated steels [31] can be various calcium aluminate phases ($xCaO.yAl_2O_3$), Al_2O_3, MgO, magnesium aluminate spinel $MgO.Al_2O_3$, sulfides CaS, MnS, and nitrides TiN, and BN. Particularly, the detection of nitrides is important because they degrade various properties of steels. For example, TiN inclusions with several microns in size tend to trigger cleavage fracture [8]. Although B addition to heat-resistant steels significantly enhances their creep strength, BN precipitation prevents the enhancement of creep strength in steels containing N, such as ferritic heat-resistant steels with a high chromium content, because of the reduction in the amount of B dissolved in the steel [8]. Moreover, B is a known as a micro-alloying element for enhancing the hardenability of steels [32]. However, the effect is only noticed if B is solute in the steel matrix, rather than in precipitates or inclusions, e.g. h-BN. Detecting BN with SEM-EDS is challenging as both B and N are light elements. Therefore, the successfulness of the B micro-alloying could be left undetected in traditional inclusion analyses, where analysis time per particle is in the range of seconds [33]. These challenges re-

quire advanced characterizations with local probe in order to manipulate them towards clean steel.

Spectro-microscopically, the first observation is that the additional B may result in more BN which shows strong interaction with a few Ca^{2+}. These Ca^{2+}-based inclusions also stabilize with TiN. Such interactions of Ca^{2+}-containing phases with BN and TiN also evidence the favorable irregular coordination of Ca^{2+}, observed by Ca $L_{2,3}$-edge XAS. However, no interaction between TiN and BN within the studied steel matrix has been found. As shown in PEEM images and calculated by DFT, pure BN inclusions or BN inclusions containing small amount of Ti are mainly sphere-shaped favoring minimum energy configuration. These observations are also in line with recent experimental observations that inclusions in steels with low concentration of Ti are mostly spherical [34]. DFT simulations facilitate the experimental conclusion on the composition of the inclusions of various sizes. Ca-based NMIs are found to be of a bigger size and most likely to form compared to B-based NMIs. Such observations may help to investigate the optimized interfacial interaction among various inclusions as well as steel matrix.

In summary, the results presented in this work localize, identify and characterize (shape, size, distribution, local spectro-microscopic behavior) several NMIs embedded within ultra-high-strength steels via X-PEEM and first-principles calculations. X-PEEM investigation on four different inclusions suggests the formation of both the Boron nitride and titanium nitride, however without any interaction in the two. The observed irregular coordination of central Ca through Ca $L_{2,3}$-edge XAS spectra also matches the observation that Ca^{2+}-based phases stabilizes with either via TiN or BN but not with both together. The first-principle calculations further facilitate these experimental observations on the composition of the inclusions of various sizes. A few include the prediction of stable bigger size Ca^{2+}-based phases and an unfavorable combination of h-BN and TiN. This study provides a pathway to optimize interaction mechanism among various inclusions and steel matrix towards cleaner steel production.

Authors' contribution

H.S.: problem planning, conceptualization, data analysis and writing; T.A.: samples preparation, SEM and writing; A.A.K.: DFT calculations and writing; S.A.A.: DFT discussion; S.W.: HE-SXRD data processing; L.Z., B.S., Y.N., and A.Z.: X-PEEM measurements on various inclusions; F.M.F. de Groot: XAS data analysis discussion; W.C. initiation and implication of X-PEEM in OU, discussion and revision of the manuscript; M.H. and T.F. discussion and commenting on the manuscript.

Declaration of Competing Interest

The authors declare no competing interests.

Acknowledgment

Authors acknowledge Academy of Finland grant #311934 for the financial support. We also thank the crew of the MAX IV laboratory for their support during the beamtime operation. Authors also acknowledge Dr. Ulrich Lienert for providing HE-SXRD data using P21.2 beamline, PETRA III, Germany. Authors would like to thank Mr. Tun Tun Nyo for the assistance in sample preparation for SEM and X-PEEM, and the Centre for Material Analysis, University of Oulu is also acknowledged for in-house characterizations. Dr. Harishchandra Singh also thanks Ms. Parisa Talebi and Dr. Ekta Rani for their assistance in compiling the draft. Computing resources were provided by *CSC - IT Center for Science*, Finland.

Supplementary materials

Supplementary material associated with this article can be found, in the online version, at doi:10.1016/j.scriptamat.2021.113791.

References

[1] H. Suito, R. Inou, ISIJ Int. 36 (1996) 528–536.
[2] I. Jung, S.A. Decterov, A.D. Pelton, ISIJ Int. 44 (2004) 527–536.
[3] L. Zhang, B.G. Thomas, Metall. Mater. Trans. B 37B (2005) 733–761.
[4] P. Rocabois, J.N. Pontoire, J. Lehmann, H. Gaye, J. Non Cryst. Solids 282 (2001) 98–109.
[5] A.B. Schmiedt, H.H. Dickert, W. Bleck, U. Kamps, Acta Mater. 95 (2015) 1–9.
[6] Y. Wang, A. Karasev, P.G. Jönsson, Steel Res. Int. 91 (2020) 1900669.
[7] D. Janis, R. Inoue, A. Karasev, P.G. Jönsson, Adv. Mater. Sci. Eng. 2014 (2014) 1–7.
[8] S. Imashuku, K. Wagatsum, Surf. Interface Anal. 51 (2019) 31–34.
[9] B. Bandi, B. Santillana, W. Tiekink, N. Koura, P. Srirangam, Ironmak. Steelmak. 47 (2020) 47–50.
[10] Z. Peng, J. Liu, F. Huang, Q. Hu, Z. Cheng, S. Liu, Steel Res. Int. 89 (1–8) (2018) 1700566 (2018).
[11] Y. Cao, G. Li, Y. Hou, N. Moelans, M. Guo, Phys. B Condens. Matter 558 (2019) 10–19.
[12] S. Lin, H. Yang, Y. Su, K. Chang, C. Yang, S. Lin, J. Alloys Compd. 779 (2019) 844–855.
[13] Y.J. Wang, P. Hu, X.L. Ma, Phys. Chem. Chem. Phys. 15 (2013) 17112–17117.
[14] X. Shi, S. Posysaev, M. Huttula, V. Pankratov, J. Hoszowska, J.C. Dousse, F. Zeeshan, Y. Niu, A. Zakharov, T. Li, O. Miroshnichenko, M. Zhang, X. Wang, Z. Huang, S. Saukko, D.L. González, S. van Dijken, M. Alatalo, W. Cao, Small 14 (2018) 1704526.
[15] G. Kresse, J. Furthmüller, Phys. Rev. B 54 (1996) 11169–11186.
[16] J.P. Perdew, K. Burke, M. Ernzerhof, Phys. Rev. Lett. 77 (1996) 3865–3868.
[17] M.M. Abdus Salam, Results Phys. 10 (2018) 934–945.
[18] F. Gyakwaa, M. Aula, T. Alatarvas, T. Vuolio, Q. Shu, M. Huttula, T. Fabritius, ISIJ Int. 60 (2020) 988–997.
[19] Q. Shu, V.V. Visuri, T. Alatarvas, T. Fabritius, Metall. Mater. Trans. B Process Metall. Mater. Process. Sci. 51 (2020) 2905–2916.
[20] P. Roese, C. Keutner, U. Berges, P. Espeter, C. Westphal, Metall. Mater. Trans. A Phys. Metall. Mater. Sci. 48 (2017) 1484–1490.
[21] Y. Rattanachai, K. Rintramee, S. Rattanasuporn, Nucl. Inst. Methods Phys. Res. B 436 (2018) 292–297.
[22] E.O. Filatova, A.S. Konashuk, S.S. Sakhonenkov, A.A. Sokolov, V.V Afanas, Sci. Rep. 7 (2017) 4541.
[23] F.M.F. de Groot, J.C. Fuggle, B.T. Thole, G.A. Sawatzky, Phys. Rev. B 41 (1990) 928–937.
[24] F.J. Himpsel, U.O. Karlsson, A.B. McLean, L.J. Terminello, F.M.F. de Groot, M. Abbate, J.C. Fuggle, J.A. Yarmoff, B.T. Thole, G.A. Sawatzky, Phys. Rev. B 43 (1991) 6899–6907.
[25] M.E. Fleet, X. Liu, Am. Mineral. 94 (2009) 1235–1241.
[26] G. Geng, R.J. Myers, A.L.D. Kilcoyne, J. Ha, P.J.M. Monteiro, Am. Mineral. 102 (2017) 900–908.
[27] Q. Li, Y. Ge, G. Geng, S. Bae, P.J.M. Monteiro, J. Nanomater. 2015 (2015) 215371.
[28] H.C. Choi, S.Y. Bae, W.S. Jang, J. Park, J. Phys. Chem. B 109 (2005) 7007–7011.
[29] N.L. Mcdougall, J.G. Partridge, R.J. Nicholls, S.P. Russo, D.G. Mcculloch, Phys. Rev. B 96 (2017) 144106.
[30] J. Wang, Z. Wang, H. Cho, M.J. Kim, T.K. Sham, X. Sun, Nanoscale 7 (2015) 1718–1724.
[31] H. Tervo, A. Kaijalainen, T. Pikkarainen, S. Mehtonen, D. Porter, Mater. Sci. Eng. A 697 (2017) 184–193.
[32] É. Dénes, A.L. Tóth, E.-R. Fábián, Mater. Sci. Form. 659 (2010) 295–300.
[33] B.G. Bartosiaki, J.A.M. Pereira, W.V. Bielefeldt, A.C.F. Vilela, J. Mater. Res. Technol. 4 (2015) 235–240.
[34] Z. Peng, J. Liu, F. Huang, Q. Hu, C. Cao, S. Hou, Int. J. Hydrog. Energy 45 (2020) 12616.